Available online at www.sciencedirect.com

ScienceDirect

journal homepage: www.elsevier.com/locate/he

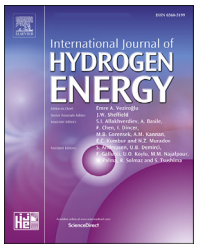

A fast two-phase non-isothermal reduced-order model for accelerating PEM fuel cell design development

Yuwei Pan [a], Huizhi Wang [b,*], Nigel P. Brandon [a,**]

[a] Department of Earth Science and Engineering, Imperial College London, London SW7 2AZ, UK
[b] Department of Mechanical Engineering, Imperial College London, London SW7 2AZ, UK

HIGHLIGHTS

- A reduced-order model for PEM fuel cells is developed.
- The model is two orders of magnitude faster than the conventional 1D model.
- The model results agree well with the 1D model.
- The influence of the membrane electrode assembly design is studied.
- CL thickness is the dominant factor at low current density.

ARTICLE INFO

Article history:
Received 21 April 2022
Received in revised form
10 August 2022
Accepted 5 September 2022
Available online 24 September 2022

Keywords:
Proton exchange membrane fuel cell
Reduced order model
Two-phase flow
Cell performance
Cell design

ABSTRACT

A reduced-order model (ROM) is developed for proton exchange membrane fuel cells (PEMFCs) considering the non-isothermal two-phase effects, with the goal of enhancing computational efficiency and thus accelerating fuel cell design development. Using analytical order reduction and approximation methods, the fluxes and source terms in conventional 1D conservation equations are reduced to six computing nodes at the interfaces between each cell component. The errors associated with order reduction are minimized by introducing new approximation methods for the potential distribution, the transport properties, and the membrane hydration status. The trade-off between model accuracy and computational efficiency is studied by comparing the simulation results and computational times of the new model with a full 1D model. The new model is nearly two orders of magnitude faster without sacrificing too much accuracy (<4% difference) compared to the 1D model. The new model is then used to analyze the influence of the membrane electrode assembly (MEA) design on cell performance and internal state distributions, offering insights into MEA structural optimization. The model can be readily extended to account for more detailed physico-chemical processes, such as Knudsen diffusion or the influence of micro-porous layers, and it can be an effective tool for understanding and designing PEMFCs.

* *Corresponding author.*
** *Corresponding author.*
E-mail addresses: huizhi.wang@imperial.ac.uk (H. Wang), n.brandon@imperial.ac.uk (N.P. Brandon).

https://doi.org/10.1016/j.ijhydene.2022.09.044

Nomenclature

Symbols

a	Surface area, $m^2\ m^{-3}$
A	Tafel constant, $V\ K^{-1}$
B	Concentration constant, $V\ K^{-1}$
c	Gas concentration, $mol\ m^{-3}$
d	Size of catalyst layer agglomerates, m
D	Diffusion coefficients, $m^2\ s^{-1}$
E	Potential, V
Er	Agglomerate effective factor
f	Ionomer water volume fraction
F	Faraday constant, $C\ mol^{-1}$
g	Ionomer water adsorption/desorption rate, $cm\ s^{-1}$
h	Henry's constant, $Pa\ m^3\ mol^{-1}$
H	Enthalpy, $kJ\ mol^{-1}$
ΔH	Enthalpy for water formation, $kJ\ mol^{-1}$
i	Current density, $A\ m^{-3}$ or $A\ cm^{-2}$
I	Output current density, $A\ m^{-2}$
j	Flux, $A\ m^{-2}$, $mol\ m^{-2}\ s^{-1}$, $W\ m^{-2}$
k	Thermal conductivity, $W\ K^{-1}$
K	Hertz-Knudsen mass transport coefficients, $m\ s^{-1}$
L	Thickness, m
M	Molar mass, $g\ mol^{-1}$
n	Number of segments
P	Pressure, Pa
q	Cathode half cell reaction constant, s^{-1}
r	Resistance, $\Omega\ m^2$
R	Gas constant, $J\ mol^{-1}\ K^{-1}$
RH	Relative humidity
$RMSE$	Root mean square error
s	Liquid water saturation
S	Source term
ΔS	Entropy change, $J\ mol^{-1}\ K^{-1}$
T	Temperature, K
U	Potential, V
V	Molar volume, $m^3\ mol^{-1}$
x	Coordinate, m
X	Molar fraction

Greeks

α	Symmetry factor
β	Thiele modulus
γ	Phase change rate, s^{-1}
Γ	Transport properties
δ	Thickness, m
ε	Volume fraction
η	Overpotential, V
θ	Coverage ratio
κ	Liquid water permeability, m^2
λ	Ionomer water content
μ	Liquid water viscosity, mPa s
ξ	Electro-osmotic drag coefficient
σ	Electron/proton conductivity, $S\ m^{-1}$
τ	Tortuosity
ϕ	Potential, V
ϕ	Scalar

Subscripts

0	Reference
1D	1D model
a	Adsorption
A	Anode
abs	Absolute
act	Activation
AGC	Anode gas channel
agg	agglomerate
ave	Average
c	Condensation
C	Cathode
cap	Capillary
CL	Catalyst layer
CGC	Cathode gas channel
d	Desorption
e	Evaporation
E	Electron
eff	effective
eq	Equilibrium
film	Ionomer film
GDL	Gas diffusion layer
h	Heat
H_2	Hydrogen
H_2O	Water (vapor)
i	Species
I	Ionomer
l	Left boundary
L	Limit
lg	Liquid gas interface
lumped	Lumped
m	Membrane
mob	mobile
O_2	Oxygen
ocv	Open circuit voltage
ORR	Oxygen reduction reaction
p	Pore
P	Proton
PtO	Platinum oxide
r	Right boundary
red	Reduced
ref	Reference
ROM	Reduced order model
w	Liquid water
λ	Ionomer water content

Abbreviations

CL	Catalyst layer
ECSA	Electrochemical surface area
GC	Gas channel
GDL	Gas diffusion layer
HOR	Hydrogen oxidation reaction
MEA	Membrane electrode assembly
MEM	Membrane
ODE	Ordinary differential equation
ORR	Oxygen reduction reaction
PDE	Partial differential equation

PEM	Proton exchange membrane	RMSE	Root mean square error
PEMFC	Proton exchange membrane fuel cell	ROM	Reduced order model
RH	Relative humidity		

Introduction

Proton exchange membrane (PEM) fuel cells are regarded as promising energy conversion devices for mobile and stationary applications due to their many advantages such as high efficiency, low emissions, and decoupled power and energy capacity [1,2]. Despite significant advances in PEM fuel cell technology over the past few decades, further improvements in performance, durability, and cost are still required to unlock their full commercial potential [1]. Mathematical models have been extensively used as a complementary tool to experiments for fuel cell development because they can provide insights into fundamental processes which are not obtainable from experiments, and can accelerate fuel cell design optimization without the need of creating and testing numerous fuel cell prototypes. Although various microscopic and mesoscopic models have been developed for resolving real microstructures and small-scale processes in fuel cells [3–5], these models are seldom used to simulate full cell operation due to the large difference in length scales and associated heavy computational cost. To model a full cell, macroscopic models are usually used, which can be classified into three categories: Physics-based continuum models [6,7], data-driven models [8,9], and empirical models [6,10].

The physics-based continuum models consider the partial differential equations (PDEs) or ordinary differential equations (ODEs) of various scalars for a computational domain, which can be 1D [7], 2D [11–13], or 3D [14,15]. By introducing the conservation equations for certain mechanisms, the continuum model can include multiple electrochemical and transport processes of the cell, like transport of reactants, water, heat, local potential in the electrode and ionomer phase, etc., which enable these models to capture the behavior of PEMFCs under a wide range of working conditions. Vetter and Schumacher [7] developed an open-source 1D model for PEMFCs based on macro-homogeneous modelling approaches. The model considered multiple influencing factors such as temperature and humidity and was later used to investigate the scattered material properties in the literature [16,17]. While most of the continuum models use effective diffusion coefficients approximated with tortuosity factors, some studies also tried to employ coefficients calculated with real electrode geometries to consider the coupling between effective diffusion and reaction [18,19]. In addition to the transport of reactants in pores, diffusion in the thin ionomer film covering the Pt/C particles was also found to have significant influence on the oxygen transport resistance [20]. Sánchez-Ramos et al. [20] developed a 1D CL model with an additional local oxygen transport sub-model to capture the cell performance at low Pt loading, and a following parametric study [21] showed that thin CLs, high carbon volume fraction, and open pores are beneficial for cell design with low Pt loading. Since the Pt/C particles and ionomer in CL can have an agglomerate-type structure [22], some studies also tried to introduce the coupling between reaction and diffusion inside the agglomerates to the 1D continuum model. These studies often consider the agglomerates as spheres covered by thin ionomer films [23,24] and the secondary pores inside the agglomerates are usually ignored [23] or assumed to be filled with liquid water [24].

On the other hand, the 2D and 3D models can also include the land/channel effect [14], concentration gradients through the channel [25], and in-plane transport phenomena [11], which may improve their accuracy for large cells with low stoichiometries. In the study of Ye and Nguyen [14], a 3D model was established using experimentally measured capillary pressure curves. The spatial heterogeneous water saturation distribution can be observed from the simulation result and was found to have a significant influence on the overall cell temperature. Gößling et al. [26] developed a 2D + 1D PEMFC stack model to study the water management of fuel cell systems. The simulation results showed that the membrane (MEM) is better saturated when the reactants are in a counter-flow configuration, and that the temperature gradient can have a different effect for cells operating under different flow configurations. Comparing to 2D models, the 3D models also allow the use of real flow channel structures and have been extensively used for studying the transport process inside the gas channels [27], as well as the optimization of flow field geometry [28–31]. In the study of Jabbary et al. [30], a 3D model is used to simulate the performance of rhombus designed PEMFCs. Three types of rhombus designs are compared to a base design, and both were found to have a positive influence on cell performance. With a 3D CFD approach, Ashrafi et al. [29] studied different channel geometries, and a flow field with a pin design showed higher current density and power compared to three other designs. However, while being able to achieve higher accuracy, these models incur relatively heavy computational cost as the continuum models have several coupled conservation equations and require a mesh grid for each cell component.

Data-driven methods can describe the nonlinear characteristics of PEMFCs without prior knowledge of any mechanism-based equations, thus the complexity of these models can be reduced significantly compared to the continuum models [32]. To date, various data-driven approaches, such as artificial neural networks [8,9,33] and support vector machines [33], have been developed for PEMFCs. Since these models are only based on the common patterns of the input-output relationship of experimental datasets without considering any detailed mechanisms, they can be readily applied to PEMFC stacks without increasing computational power demand [34]. However, their accuracy is strongly dependent on the quantity and quality of experimental data, and their application is also limited to the range of working conditions where data is provided.

As shown in Eq. (1) [35], a typical empirical model describes cell polarization by considering four terms: the reversible potential, ohmic loss, activation loss, and concentration loss [6,35].

$$U = U_{ocv} - rI - AT\ln\left(\frac{I}{i_0}\right) + BT\ln\left(1-\frac{I}{I_L}\right) \quad (1)$$

where U is the output voltage, U_{ocv} is the open-circuit voltage, r is the ohmic resistance, I represents the output current density, A and B are the activation and concentration constants, T is the operating temperature, and i_0 and I_L are the exchange current density and limiting current density, respectively. This empirical equation includes the three most significant potential loss sources and can be parameterized to capture the polarization curves of PEMFCs measured by experiments. However, since this model ignores many important factors, like membrane hydration status, water transport, etc., once parameterized its accuracy is limited to a certain range of working conditions [6]. Although the accuracy and generalization capability of 0D empirical models is low, their low computational demand is still favored by several types of applications such as lifetime assessment [36] and large-scale simulation based on the hierarchical method [37,38].

To improve performance over a wider range of working conditions, various efforts have been made to introduce more detailed mechanisms into the 0D empirical model. Das et al. [10] developed an analytical catalyst layer (CL) electrochemical sub-model and integrated it into the traditional empirical model described in Eq. (1), together with O_2 transport in flooded/dry electrodes. Based on this analytical CL model, Jiang et al. [39] further introduced the transport of heat and mass into the model with homogenized flux rates. This model also tried to include the phase change of water by using a vapor saturated electrode and transferring all remaining water into liquid form. Rahman et al. [40] used a similar approach to model gas transport, but they further introduced non-Fickian transport resistances determined by limiting current experiments as well as an ordinary differential equation to describe the water transport in the membrane, and the proton transport loss was modelled with another analytical approach based on the studies of Thompson et al. [41] and Neyerlin et al. [42]. With the above modifications, the included mechanisms in these 0D models approach those found in 1D continuum models, which enables them to work under extended ranges of temperature, back pressure, and humidity conditions, and the mechanistic equations in these models allow them to use experimentally measured material properties to avoid complex parameterization processes. However, since these models are still based on several common assumptions including uniformly distributed scalars, transport properties and source terms in each component, their simulation results can severely deviate from a full 1D model of PEMFCs, even if they have the same descriptions of the reaction and transport mechanisms and model parameters.

To minimize computational cost without sacrificing too much model accuracy, this study starts from a different perspective. Using analytical order reduction and approximation methods, the fluxes and source terms in the conventional 1D conservation equations are reduced to six computing nodes at the interfaces between each cell component. The errors associated with order reduction are minimized by introducing new approximation methods for the potential distribution, transport properties and the membrane hydration status. The trade-off between model accuracy and computational efficiency is studied by comparing the simulation results and computational times of the new model with a full 1D model. The new model is found to be nearly two orders of magnitude faster compared to the 1D model, and the discrepancy between the polarization curves simulated by the two models is less than 4% for most of the working conditions. This reduced order model (ROM) is then used to analyze the influence of the membrane electrode assembly (MEA) design on cell performance and internal state distributions, offering insights into MEA structural optimization. The model can be readily extended to account for more detailed physico-chemical processes, such as Knudsen diffusion, the influence of microporous layer, or degradation. The gas channels (GC) structure or channel-rib geometry can also be considered by integrating this model into hierarchical modelling frameworks. The modelling approach presented in this paper can therefore be an effective tool for understanding and designing PEM fuel cells.

Model development

1D PEM fuel cell model

The non-isothermal two-phase PEM fuel cell model developed by Vetter and Schumacher [7] is adopted as a reference model. The model is based on a macro-homogeneous approach and implemented in one dimension considering the dominating through-plane transport processes in a five-layer MEA with gas channels simplified as boundaries (Fig. 1 (a)). The major assumptions of this model include: one-dimension through plane transport, steady-state, ideal gas, isobaric, Fickian diffusion, convection neglected and homogeneous porous media. The model consists of eight conservation equations as follows:

$$\text{Electron conservation } \nabla\cdot(\sigma_E\nabla\phi_E) + S_E = 0 \quad (2)$$

$$\text{Proton conservation } \nabla\cdot(\sigma_P\nabla\phi_P) + S_P = 0 \quad (3)$$

$$\text{Energy conservation } \nabla\cdot(k\nabla T) + S_T = 0 \quad (4)$$

$$\text{Gaseous species conservation } (i = H_2,\ O_2,\ \text{or } H_2O(g)) \quad \nabla\cdot\left(D_i\frac{P}{RT}\nabla X_i\right) + S_i = 0 \quad (5)$$

$$\text{Liquid water conservation } \nabla\cdot\left(\frac{\kappa}{\mu V_w}\frac{\partial P_{cap}}{\partial s}\nabla s\right) + S_s = 0 \quad (6)$$

$$\text{Water conservation in the ionomer phase} \quad \nabla\cdot\left(D_\lambda\nabla\lambda - \frac{\xi}{F}j_P\right) + S_\lambda = 0 \quad (7)$$

where ϕ_E, ϕ_P, T, X_i, s and λ respectively denote the potential in electrode phase, the potential in electrolyte phase, temperature, the molar fraction of species i, liquid water saturation,

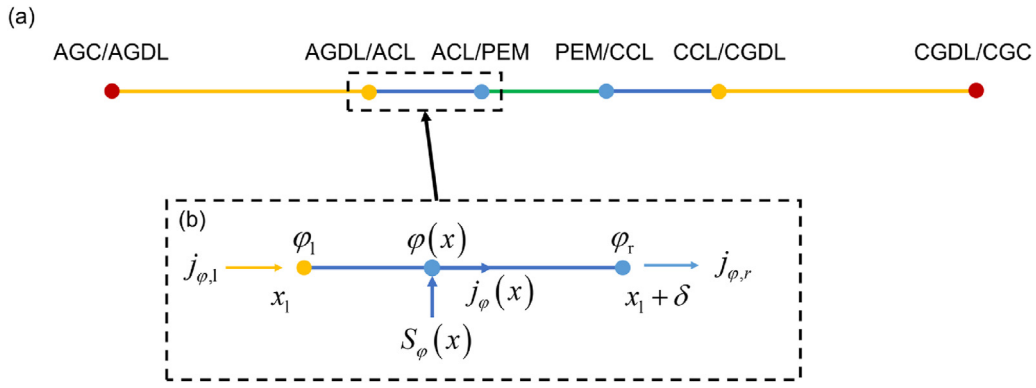

Fig. 1 – A schematic illustration of the five-layer MEA, the computing nodes, and the flux conservation inside a subdomain: (a) the five-layer MEA and the six computing nodes at the interfaces between and boundaries of the cell components; (b) the flux conservation of a scalar in a subdomain.

and water content in the ionomer; σ_E and σ_P respectively are the electronic and ionic conductivity; k is the thermal conductivity; D_i represents the diffusion coefficient of species i, P is the pressure, R is the ideal gas constant, κ is the liquid water permeability, μ is the liquid water viscosity, V_w is the molar volume of liquid water, P_c is the capillary pressure, D_λ is the water diffusivity in ionomer and ξ is the electro-osmotic drag coefficient. The physico-chemical properties, the source terms, S_E, S_P, S_T, S_i, S_s, and S_λ, as well as the boundary conditions are summarized in Tables 1–3. The property relations and the source term formulations have been well discussed and justified elsewhere [7] and are therefore not detailed here.

Model order reduction for transport processes

The 1D fuel cell model is reduced to six computing nodes located at the boundaries of interfaces between the MEA layers as shown in Fig. 1 (b). For each layer, the conservation laws can be reduced to

$$j_\phi(x) = j_{\phi,l} + \int_{x_l}^{x_l+\delta} S_\phi dx \tag{8}$$

where j is the scalar flux, the subscript ϕ is the scalar index (= ϕ_e, ϕ_P, T, X_i, s, and λ), and δ is the thickness of the layer. Assuming linearly distributed source terms, Eq. (8) can be rewritten as:

$$-\Gamma_\phi \frac{\phi_r - \phi_l}{\delta} = j_{\phi,l} + \left(\frac{S_{\phi,r}}{6} + \frac{S_{\phi,l}}{3}\right)\delta \tag{9}$$

for $\phi = \phi_e$, ϕ_P, T, X_{H2}, X_{O2}, X_{H2O}, where Γ is the corresponding transport coefficient dependent on the states of the two neighboring computing nodes.

Apart from the diffusion flux ($D_\lambda \nabla\lambda$), water transport in the ionomer phase can also be affected by the electro-osmotic drag. Integrating Eq. (8) for the ionomer water transport thus gives:

$$\frac{2.5}{22F}(\lambda j_P)_{ave} - \frac{D_\lambda}{V_m}\frac{\lambda_r - \lambda_l}{\delta} = j_{\lambda,l} + \left(\frac{S_{\lambda,r}}{6} + \frac{S_{\lambda,l}}{3}\right)\delta \tag{10}$$

Averaged transport properties

The transport properties of protons, liquid water in the GDL, and water in the ionomer can change nonlinearly and dramatically across the component layers. However, the distributions of the scalars themselves are relatively linear compared to their transport properties. Therefore, these transport properties can be computed by discretizing the component layer to n segments and using the linearized scalars, which gives

$$\Gamma_{lumped} = \frac{n}{\sum_{i=1}^{n} \frac{1}{\Gamma\left(\phi_l + \frac{2i-1}{2n}(\phi_r - \phi_l)\right)}} \tag{11}$$

Considering a trade-off between the simulation accuracy and computational cost, the number of segments n is set to be 10.

For other transport properties, the gradients are relatively small, so they are approximated as:

$$\Gamma = \frac{2}{\frac{1}{\Gamma_l} + \frac{1}{\Gamma_r}} \tag{12}$$

Electrochemical model

The electrode kinetics can be described using the Butler-Volmer equation [10]. At the cathode, due to the slow oxygen reduction reaction kinetics and relatively high proton and electronic conductivities, the proton/electron flux is approximately linearly distributed, and the potential gradients are small in the ionomer and carbon phase. Therefore, the Butler-Volmer kinetics can be simplified and rearranged to give the expression of the cathode activation overpotential as follows:

$$\eta_{act,C} = \frac{RT_{ave}}{F}\sinh^{-1}\left(\frac{I}{2\delta_{CL} i_{0,ave}}\right) \tag{13}$$

where T_{ave} and $i_{0,ave}$ are the temperature and exchange current density in the cathode CL, which are assumed to be the arithmetic average of the two neighboring nodes. By neglecting the potential drop in the carbon phase [10], the total overpotential associated with the cathode CL is the sum of the

Table 1 – Physico-chemical properties (All properties in this table are kept the same as the reference model and are taken from Ref. [7]).

Physical and transport properties	
Molar enthalpy of ionomer water adsorption/desorption, H_{ad}, (kJ/mol)	42
Molar enthalpy of water evaporation/condensation, H_{ec}, (kJ/mol)	42
Thermal conductivity for GDL, CL, and membrane, k_{GDL}, $k_{CL,}$ k_m (W/m K)	1.6, 0.27, 0.3
Diffusion coefficient of species I, for i = H_2, O_2, H_2O(g), D_i (cm^2/s)	$D_i = \frac{\varepsilon_p}{\tau^2}(1-s^3)D_{i,ref}\left(\frac{T}{T_{ref}}\right)^{1.5}\frac{P_{ref}}{P}$
Reference diffusion coefficient of species i, for i = H_2, O_2, H_2O(g), $D_{i,ref}$ (cm^2/s)	1.24 (hydrogen in water vapor), 0.28 (oxygen in air), 1.24 (water vapor in hydrogen), 0.36 (water vapor in air)
Gas concentration, C (mol/m^3)	$c = \frac{P}{RT}$
Pore tortuosity, τ	1.6
GDL porosity, ε_p	0.76
Reference temperature, T_{ref} (K)	353.15
Reference pressure, P_{ref} (atm)	1
Water saturation pressure, P_{SAT} (Pa)	$\ln\left(\frac{P_{SAT}}{1\ Pa}\right) = 23.1963 - \frac{3816.44\ K}{T - 46.13\ K}$
Saturated molar fraction of water vapor, X_{SAT}	$X_{SAT} = \frac{P_{SAT}}{P}$
Water vapor molar fraction at GDL/GC interface, $X_{H2O,A}$ and $X_{H2O,C}$	$\begin{cases} X_{H_2O,A} = \frac{RH_A P_{SAT}(T_A)}{P_A} \\ X_{H_2O,C} = \frac{RH_C P_{SAT}(T_C)}{P_C} \end{cases}$
Oxygen molar fraction at CGDL/CGC interface, $X_{O2,c}$	$X_{O_2,C} = 0.21(1 - X_{H_2O,C})$
Hydrogen molar fraction at AGDL/AGC interface, $X_{H2,A}$	$X_{H_2,A} = 1 - X_{H_2O,A}$
Condensation/evaporation rates, γ_e, γ_c (1/s)	$\begin{cases} \gamma_e = K_e a_{lg} s_{red} \\ \gamma_c = K_c a_{lg}(1 - s_{red}) \end{cases}$
Effective liquid-gas interfacial surface area, a_{lg} (m^2/m^3)	2×10^6
Hertz-Knudsen mass transport coefficients, K_e, K_c (m/s)	$\left.\begin{matrix} K_e \\ K_c \end{matrix}\right\} = \sqrt{\frac{RT}{2\pi M_w}} \times \left\{\begin{matrix} 5 \times 10^{-4} \\ 6 \times 10^{-3} \end{matrix}\right.$
Molar mass of water, M_w (g/mol)	18
Reduced saturation, s_{red}	$s_{red} = \frac{s - s_C}{1 - s_C}$
Liquid water viscosity, μ (mPa s)	$\ln\left(\frac{\mu}{1\ mPa\ s}\right) = -3.63148 + \frac{542.05\ K}{T - 144.15\ K}$
Liquid water permeability, κ (m^2)	$\kappa = (10^{-6} + s_{red}^3)\kappa_{abs}$
Absolute permeability of GDL and CL, κ_{abs} (m^2)	6.15×10^{-12}, 10^{-13}
Capillary pressure, P_{cap} (Pa)	$\frac{P_{cap}}{1\ Pa} = -0.00011\exp[-44.02(s - 0.496)] + 278.3\exp[8.103(s - 0.496)] - 191.8$
Liquid water saturation at GDL/channel interface, s_C	0.12
Water diffusion coefficient in ionomer, D_λ (m^2/s)	$D_\lambda = \varepsilon_I^{1.5}\frac{3.842\lambda^3 - 32.03\lambda^2 + 67.74\lambda}{\lambda^3 - 2.115\lambda^2 + 33.013\lambda + 103.39}10^{-10}\frac{m^2}{s} \times \exp\left[\frac{20kJ/mol}{R}\left(\frac{1}{T_{ref}} - \frac{1}{T}\right)\right]$
Electro-osmotic drag coefficient, ξ	$\xi = \frac{2.5}{22}\lambda$
Equilibrium ionomer water content, λ_{eq}	$\lambda_{eq} = 0.043 + 17.81RH - 39.85RH^2 + 36.0RH^3$
Relative gas humidity, RH	$RH = \frac{X_{H_2O}}{X_{SAT}}$
Ionomer water adsorption/desorption rate, g_a, g_d (cm/s)	$\left.\begin{matrix} g_a \\ g_d \end{matrix}\right\} = f\exp\left[\frac{20\ kJ/mol}{RT}\right] \times \left\{\begin{matrix} 3.53 \times 10^{-3}\ cm/s \\ 1.42 \times 10^{-2}\ cm/s \end{matrix}\right.$
Volume fraction of water in ionomer, f	$f = \frac{\lambda V_w}{\lambda V_w + V_m}$
Molar volume of liquid water, V_w (cm^3/mol)	18/0.978
Molar volume of dry membrane, V_m (cm^3/mol)	1020/1.97
Electrochemical properties	
Current density, i (A/m^3)	$i = ai_0\left(\exp\left[\frac{F}{RT}\eta\right] - \exp\left[-\frac{F}{RT}\eta\right]\right)$
Surface overpotential, η (V)	$\eta = \begin{cases} \phi_e - \phi_p - U_0 & \text{in ACL} \\ U_0 - \phi_e + \phi_p & \text{in CCL} \end{cases}$

(continued on next page)

Table 1 – (continued)

Physical and transport properties	
Reversible potential, U_0 (V)	$U_0 = \begin{cases} -\frac{T\Delta S_{HOR}}{2F} - \frac{RT}{2F}\ln\left(\frac{P_{H_2}}{P_{ref}}\right) & \text{in ACL} \\ -\frac{\Delta H - T\Delta S_{ORR}}{2F} + \frac{RT}{4F}\ln\left(\frac{P_{O_2}}{P_{ref}}\right) & \text{in CCL} \end{cases}$
Exchange current density, i_0 (A/cm^2)	$i_0 = \begin{cases} i_{0,ref}\left(\frac{P_{O_2}}{P_{ref}}\right)^{0.54} \times \exp\left[\frac{67\text{kJ/mol}}{R}\left(\frac{1}{T_{ref}} - \frac{1}{T}\right)\right] \\ 0.27\ \text{A/cm}^2 \exp\left[\frac{16\text{kJ/mol}}{R}\left(\frac{1}{T_{ref}} - \frac{1}{T}\right)\right] \end{cases}$
Enthalpy of water formation, ΔH (kJ/mol)	−285.83
Half-reaction entropy of hydrogen oxidation reaction (HOR), ΔS_{HOR} (J/mol K)	0.104
Half-reaction entropy of oxygen reduction reaction (ORR), ΔS_{ORR} (J/mol K)	−163.3
Electrical conductivity of GDL and CL, σ_E (S/m)	1250, 350
Proton conductivity of ionomer, σ_P (S/m)	$\sigma_P = \varepsilon_I^{1.5} 116 \frac{S}{m} \max\{0, f - 0.06\}^{1.5} \times \exp\left[\frac{15\text{kJ/mol}}{R}\left(\frac{1}{T_{ref}} - \frac{1}{T}\right)\right]$

activation overpotential and the ohmic loss in the ionomer phase:

$$\eta_C = \eta_{act,C} + \frac{I\delta_{CL}}{2\sigma_{P,C}} \tag{14}$$

At the anode, the changes in the overpotential and proton/electron flux can be significant because of a relatively low proton conductivity due to the less hydrated ionomer together with faster HOR kinetics. Hence, a 1D approach is used and the overpotential in the anode is described as:

$$\frac{d^2\eta_{act}}{dx^2} = -\frac{i}{\sigma_P} \tag{15}$$

with the boundary conditions:

$$\frac{d\eta_{act}}{dx}\Big|_{x=x_1} = 0 \tag{16}$$

$$\frac{d\eta_{act}}{dx}\Big|_{x=x_1+\delta} = \frac{I}{\sigma_P F} \tag{17}$$

Membrane/ionomer water content

Since there is no source term for water in the membrane, $(\lambda j_P)_{ave}$ in the membrane can be approximated as:

$$(\lambda j_P)_{ave} = \lambda_{ave} I \tag{18}$$

The water content of the membrane, λ, is solved analytically from Eq. (10) with the boundary condition shown in Eq. (20):

$$\lambda(x) = \left(\lambda_1 - \frac{22Fj_{\lambda,1}}{2.5I}\right)\exp\left(\frac{2.5I}{22FD_\lambda}x\right) + \frac{22Fj_{\lambda,1}}{2.5I} \tag{19}$$

$$\lambda|_{x=x_1} = \lambda_1 \tag{20}$$

Integrating Eq. (19) across the membrane thickness and dividing it by the membrane thickness gives the average water content in the membrane:

$$\lambda_{ave} = \frac{22FD_\lambda}{2.5I\delta_{PEM}}\left(\lambda_1 - \frac{22Fj_{\lambda,1}}{2.5I}\right)\left[\exp\left(\frac{2.5I}{22FD_\lambda}\delta_{PEM}\right) - 1\right] + \frac{22Fj_{\lambda,1}}{2.5I} \tag{21}$$

Assuming activation overpotential is constant in the catalyst layer of the cathode, $(\lambda j_P)_{ave}$ in the cathode CL can be related to the current which is linearly dependent on the coordinate x:

$$(\lambda j_P)_{ave} = \left(\frac{\lambda_l}{3} + \frac{\lambda_r}{6}\right)I \tag{22}$$

By neglecting the potential drop in the carbon phase, $(\lambda j_P)_{ave}$ in the anode CL can be approximated as:

$$(\lambda j_P)_{ave} = \frac{\sum_{i=1}^{n} j_{P,i}\left(\lambda_l + \frac{2i-1}{2n}(\lambda_r - \lambda_l)\right)}{n} \tag{23}$$

where $j_{P,i}$ is the proton flux at $x = (2i - 1)\delta/n$.

Model parameters and numerical procedures

The governing equations are organized into four sub-models, namely the reactant diffusion model (Eqs. (5), (9), (12)), electrochemical model (Eqs. (2), (3), (9), (11-17)), water transport model (Eqs. (5-7), (9-12), (18-23)), and thermal model (Eqs. (4), (9), (12)), and the four sub-models are coupled together with a segregated approach, as shown in Fig. 2. The CL electrochemical model and water transport model are solved numerically using self-written solvers developed based on the forward Euler method and Broyden's method respectively, and the other two sub-models are solved analytically. To validate the model with experiments, both the 1D model and the ROM are parameterized to the experimental results of Ref. [43]. The model parameters, including the cell configuration and fitted parameters, are summarized in Table 4.

Results and discussion

Model accuracy and computational efficiency

The simulated polarization curves of the developed model are compared with the conventional 1D approach under various working conditions as listed in Table 5. Since this work is based

Table 2 – Source terms for the conservation equations in each region [7].

	Anode GDL	Anode CL	Membrane	Cathode CL	Cathode GDL
S_e	0	-i	–	i	0
S_P	–	i	0	-i	–
S_T	$\sigma_E(\nabla\phi_E)^2$	$\sigma_E(\nabla\phi_E)^2+\sigma_P(\nabla\phi_P)^2+\left(i\eta-\frac{iT\Delta S_{HOR}}{2F}\right)$ $+H_{ad}\times\begin{cases}\frac{g_a}{LV_m}(\lambda_{eq}-\lambda)\text{ if }\lambda_{eq}<\lambda\\ \frac{g_d}{LV_m}(\lambda_{eq}-\lambda)\text{ if }\lambda_{eq}>\lambda\end{cases}$	$\sigma_P(\nabla\phi_P)^2$	$\sigma_E(\nabla\phi_E)^2+\sigma_P(\nabla\phi_P)^2+\left(i\eta-\frac{iT\Delta S_{ORR}}{2F}\right)$ $+H_{ad}\times\begin{cases}\frac{g_a}{LV_m}(\lambda_{eq}-\lambda)\text{ if }\lambda_{eq}<\lambda\\ \frac{g_d}{LV_m}(\lambda_{eq}-\lambda)\text{ if }\lambda_{eq}>\lambda\end{cases}$ $+H_{ec}\times\begin{cases}\gamma_e c(X_{H_2O}-X_{SAT})\text{ if }X_{H_2O}<X_{SAT}\\ \gamma_c c(X_{H_2O}-X_{SAT})\text{ if }X_{H_2O}>X_{SAT}\end{cases}$	$\sigma_E(\nabla\phi_E)^2+H_{ec}$ $\times\begin{cases}\gamma_e c(X_{H_2O}-X_{SAT})\text{ if }X_{H_2O}<X_{SAT}\\ \gamma_c c(X_{H_2O}-X_{SAT})\text{ if }X_{H_2O}>X_{SAT}\end{cases}$
S_{O2}	–	–	–	$-\frac{i}{4F}$	0
S_{H2}	0	$-\frac{i}{2F}$	–	–	–
S_{H2O}	0	$-\frac{g_a}{LV_m}(\lambda_{eq}-\lambda)\text{ if }\lambda_{eq}<\lambda$ $-\frac{g_d}{LV_m}(\lambda_{eq}-\lambda)\text{ if }\lambda_{eq}>\lambda$	–	$-\begin{cases}\frac{g_a}{LV_m}(\lambda_{eq}-\lambda)\text{ if }\lambda_{eq}<\lambda\\ \frac{g_d}{LV_m}(\lambda_{eq}-\lambda)\text{ if }\lambda_{eq}>\lambda\end{cases}$ $-\begin{cases}\gamma_e c(X_{H_2O}-X_{SAT})\text{ if }X_{H_2O}<X_{SAT}\\ \gamma_c c(X_{H_2O}-X_{SAT})\text{ if }X_{H_2O}>X_{SAT}\end{cases}$	$-\gamma_e c(X_{H_2O}-X_{SAT})\text{ if }X_{H_2O}<X_{SAT}$ $-\gamma_c c(X_{H_2O}-X_{SAT})\text{ if }X_{H_2O}>X_{SAT}$
S_s	–	–	–	$\gamma_e c(X_{H_2O}-X_{SAT})\text{ if }X_{H_2O}<X_{SAT}$ $\gamma_c c(X_{H_2O}-X_{SAT})\text{ if }X_{H_2O}>X_{SAT}$	
S_λ	–	$\frac{g_a}{LV_m}(\lambda_{eq}-\lambda)\text{ if }\lambda_{eq}<\lambda$ $\frac{g_d}{LV_m}(\lambda_{eq}-\lambda)\text{ if }\lambda_{eq}>\lambda$	0		–

Table 3 – Boundary conditions [7].

Scalars	AGC/AGDL	AGDL/ACL	ACL/MEM	MEM/CCL	CCL/CGDL	CGDL/CGC
ϕ_E	$\phi_E = 0$	continuity	$j_E = 0$	$j_E = 0$	continuity	$j_E = I$
ϕ_P	–	$j_P = 0$	continuity	continuity	$j_P = 0$	–
T	$T = T_A$	continuity	continuity	continuity	continuity	$T = T_C$
X_{O2}	–	–	–	$j_{O2} = 0$	continuity	$X_{O2} = X_{O2,C}$
X_{H2}	$X_{H2} = X_{H2,A}$	continuity	$j_{H2} = 0$	–	–	–
X_{H2O}	$X_{H2O} = X_{H2O,A}$	continuity	$j_{H2O} = 0$	$j_{H2O} = 0$	continuity	$X_{H2O} = X_{H2O,C}$
s	–	–	–	$j_s = 0$	continuity	$s = s_c$
λ	–	$j_\lambda = 0$	continuity	continuity	$j_\lambda = 0$	–

on the reduction of the 1D approach and the gas channel is not included in the model, the stoichiometry, which can be represented by the flow velocity of air/fuel, is not applicable. For simplicity, the inlet humidity and pressure are set to be the same on both the cathode and anode sides, and the first condition is defined as the base condition. Fig. 3(a) and Fig. 3(b) show the simulated polarization curves and power density, with lines and markers representing the result of the ROM and the 1D model, respectively. It can be observed that the ROM can provide nearly the same simulation results as the 1D model under a wide range of working conditions. While having similar results, our new modelling approach is much faster compared to the 1D model. The computing time of the models under the default model parameters of Ref. [7] is listed in Table 6. The ROM is around two orders of magnitude faster than the 1D model, and the efficiency of the model is significantly improved by using the self-written modelling framework.

The root mean square errors (RMSEs) of the polarization curve are further used to quantify and compare the errors. Since the results of the two models share the same voltage range while the current range is different, the error of simulated voltage under the same current is used, as shown in Eq. (24).

$$\mathrm{RMSE} = \sqrt{\frac{\sum_{i=1}^{n} \left(I_{1D}(U_i) - I_{CNM}(U_i)\right)^2}{n}} \tag{24}$$

where $I_{1D}(U_i)$ and $I_{ROM}(U_i)$ are the current densities predicted by the 1D model and ROM under U_i, respectively, and the number of points n is set to be 23, which corresponds to a voltage interval of 0.05 V. Since the current range under different working conditions can vary significantly, a normalized RMSE in percentage is also introduced to help the comparison:

$$\mathrm{RMSE}_{nor} = \sqrt{\frac{\sum_{i=1}^{n} \left(1 - \frac{I_{CNM}(U_i)}{I_{1D}(U_i)}\right)^2}{n}} \tag{25}$$

The quantified errors under the seven conditions are also shown in Table 5. The RMSE and normalized RMSE are below

Table 4 – Cell configuration and fitted model parameters.

Parameters	Symbol	Value	
		Anode	Cathode
GDL thickness (μm)	L_{GDL}	195 [43,44][a]	160 [7,43][a]
CL thickness (μm)	L_{CL}	11 [43]	11 [43]
Electrochemical surface area ($m^2\ m^{-3}$)	a	1.75×10^7 [43]	1.75×10^7 [43]
CL pore volume fraction (–)	$\varepsilon_{p,CL}$	0.3 [39]	0.3 [39]
Reaction coefficient of ORR ($A\ m^{-2}$)	$i_{0,ref}$	–	6e-8[f]
Ionomer volume fraction in CL (–)	$\varepsilon_{I,CL}$	0.4 [39]	0.4 [39]

[a] In the experiment of Ref. [43], the anode and cathode GDLs were SGL 24BCE (235 μm) and TGP H-060 (190 μm), respectively, but the compression rate was not specified. The thicknesses used in the models correspond to a moderate compression pressure of 1.4 MPa [7,44].
[f]: Fitted.

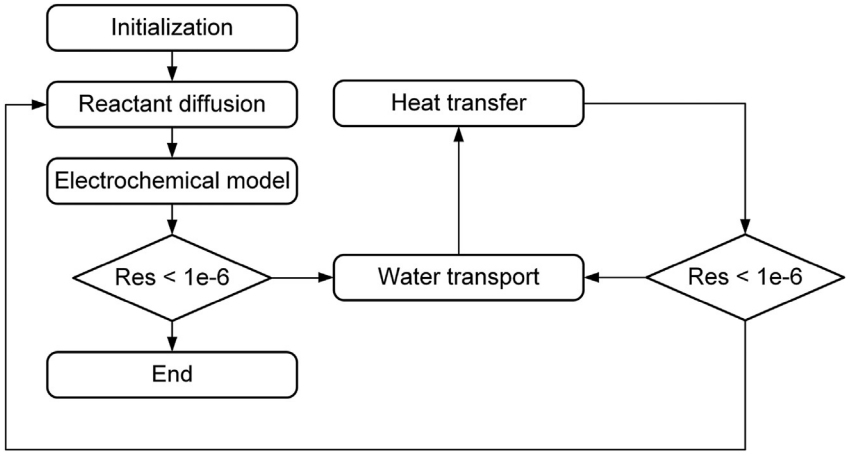

Fig. 2 – The four sub-models of the ROM and the segregated solver.

Table 5 – Simulated working conditions and error of predictions.

Condition	Temperature (K)	Pressure (kPa)	RH (–)	RMSE (A/cm2)	Normalized RMSE (%)
1 (Base condition)	**353**	**100**	**0.9**	0.05	3.5
2	**333**	100	0.9	0.04	3.4
3	**358**	100	0.9	0.05	3.4
4	353	**200**	0.9	0.05	3.2
5	353	**300**	0.9	0.05	3.0
6	353	100	**0.8**	0.06	4.2
7	353	100	**0.7**	0.06	5.0

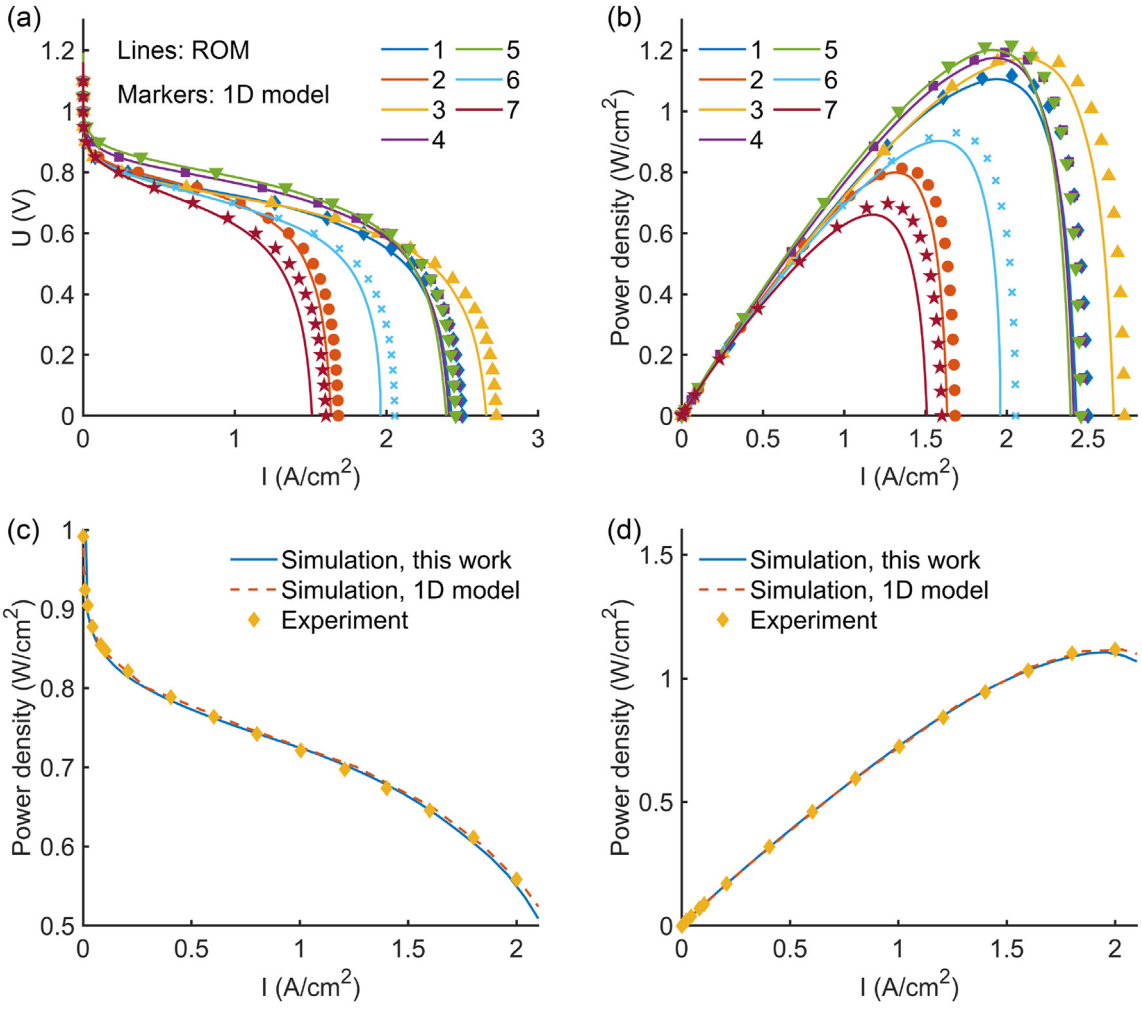

Fig. 3 – Simulation results of ROM and 1D model: (a) polarization curves simulated by ROM and 1D model, where 1–7 represents conditions 1–7, which are specified in Table 5; (b) power density curves simulated by ROM and 1D model; (c) comparison of polarization curves between simulation and experimental result of Ref. [43]; (d) comparison of power density curves between simulation and experimental result of Ref. [43].

0.06 A/cm^2 and 5%, respectively, and the largest error can be found under the least humidified condition.

As shown in Fig. 3(a), the polarization curves of the 1D model are well captured by the ROM. Compared to other conditions, the inlet pressure has the least influence on the overall performance of the cell. By increasing the inlet pressure, the cell tends to have higher voltage under low to moderate current densities because of the higher reversible potential and faster reaction kinetics. But an increased inlet pressure will also slightly lower the limiting current of the cell, possibly due to the lower diffusion coefficient of water vapor which can lead to a drier membrane. The same trend is predicted by both the ROM and the 1D model. On the other hand, the temperature has a larger impact on the polarization curves. The current output of the cell decreases significantly with a lowered temperature, and the error of the ROM under all three temperatures is kept close to 3%. Similarly, decreasing the humidity can reduce the current output of the

Table 6 – Computing time of the ROM and the 1D model.

	ROM with self-written solvers	ROM with MATLAB embedded solvers	1D model
Time per simulation (s)	0.0076	0.457	0.7
CL electrochemical model (s)	0.0011	0.055	–
Mass transport (s)	0.0065	0.402	–

cell significantly: the limiting current is decreased by more than 40% by reducing the inlet relative humidity (RH) from 0.9 to 0.7. This feature indicates that the dehydration of the membrane plays an important role in cell performance, especially at high current density. Fig. 3(b) plots the power densities simulated by the two models. It can be observed that the power density profile predicted by the ROM also agrees well with the 1D approach, especially under conditions one to five, and a slightly lower peak power density is predicted under low humidity conditions. The results of the two models are also compared with the experimental data of Ref. [43] under the base condition in Fig. 3(c) and (d), and the simulated polarization curves and power density curves of both models agree excellently with the experiment.

Internal state distributions

The internal state distributions are studied and compared with the 1D model under the base condition (condition 1) and four different current outputs representing low (0.5 A/cm^2), moderate (1.5 A/cm^2), high (1.95 A/cm^2, which is also the current at peak power) and limiting current densities (2.43 A/cm^2). Fig. 4 shows the simulated potential profiles inside the cell, which includes the potential in the carbon/electrolyte phase and the anode proton flux and potential predicted by the simplified 1D anode electrochemical model. The lines in the figure represent the result of the ROM analysis and markers stand for the result of the full 1D model. From Fig. 4(a), it can be observed that the potential barely changes in both the anode and cathode carbon phase due to their high electronic conductivity. The anode carbon phase potential is close to 0 V and is well captured, and the cathode potential approximately equals to the voltage output of the cell. The results of the ROM also agree well with the 1D approach, but a relatively large error can be seen at the limiting current density due to the rapid potential drop near the limiting current shown in Fig. 3(a). The proton conductivity of the ionomer, however, is several orders of magnitudes smaller compared to the electronic conductivity of the electrodes. As shown in Fig. 4(b), a large potential drop through the membrane can be found from 1.5 A/cm^2 to 2.43 A/cm^2. As the error in membrane potential drop is very close to the error of predicted cell voltage, it can be inferred that the slightly underestimated limiting current of the ROM is mostly due to membrane dehydration. On the anode side, the potential in the electrolyte remains nearly constant until approaching the interface between the anode CL and the membrane. Since both the potential in the carbon phase and the reversible potential of HOR are close to 0 V, the electrolyte potential can also be represented by the anode overpotential of the hydrogen oxidation reaction, which is shown in Fig. 4(c). The large gradient of anode overpotential can also lead to a highly unbalanced local HOR current density. As shown in Fig. 4(d), the rapid rise of proton flux near the anode/membrane interface is predicted by both the ROM and the 1D model, which also indicates that water transport due to electro-osmotic drag in the anode CL can be successfully captured by the ROM.

As shown in Fig. 4(b), the limiting current is due to the higher membrane resistance and the membrane proton conductivity is related to its hydration status, so it can be expected that water transport can strongly affect the accuracy of the ROM, and the results of this sub-model are shown in Fig. 5, together with the temperature gradient which can affect the saturated water vapor pressure. Fig. 5(a) shows the molar fraction of water vapor in the electrodes. From channel to membrane, the water vapor pressure tends to increase on the cathode side and decrease on the anode side. Due to the condensation effect, the water vapor pressure is limited by the saturated vapor pressure, which results in a plateau in the cathode CL until limiting current, which has an elevated temperature gradient, as shown in Fig. 5(d). The liquid water saturation in the cathode CL is shown in Fig. 5(b). Since water generated under low current conditions is limited, most of the generated water is exhausted in the vapor form and only the hydrophilic pores are saturated with liquid water.

Since the cathode CL has a higher equilibrium ionomer water content due to the higher water vapor pressure, and the osmotic drag facilitates the water transport from anode to cathode, it can be observed in Fig. 5(c) that the ionomer is significantly more hydrated on the cathode side and the lowest point of water content exists near the anode/membrane interface. The ROM effectively quantifies the ionomer water content, leading to an accurate prediction of membrane resistance until limiting current is reached. However, the conductivity of the membrane decreases dramatically when it is nearly dehydrated. At the limiting current, a small error in membrane water content at the anode/membrane interface can result in a 40% smaller membrane proton conductivity. It also results in a 62% larger membrane resistance, corresponding to a 0.25 V voltage drop, which is very close to the error of the predicted output voltage shown in Figs. 4(a) and Fig. 5(a). The overestimated membrane resistance can further lead to a higher heat generation rate and temperature gradient, which can cause a higher saturated water vapor pressure. As a result, the water vapor pressure is higher (Fig. 5(a)) and liquid water saturation is lower (Fig. 5(b)) in the cathode CL. As the equilibrium ionomer water content λ_{eq} is dependent on the local relative humidity (X_{H2O}/X_{sat}), and the saturated water vapor pressure X_{sat} increases significantly with temperature, the overestimated temperature rise can further facilitate the prediction of membrane dehydration in the ROM.

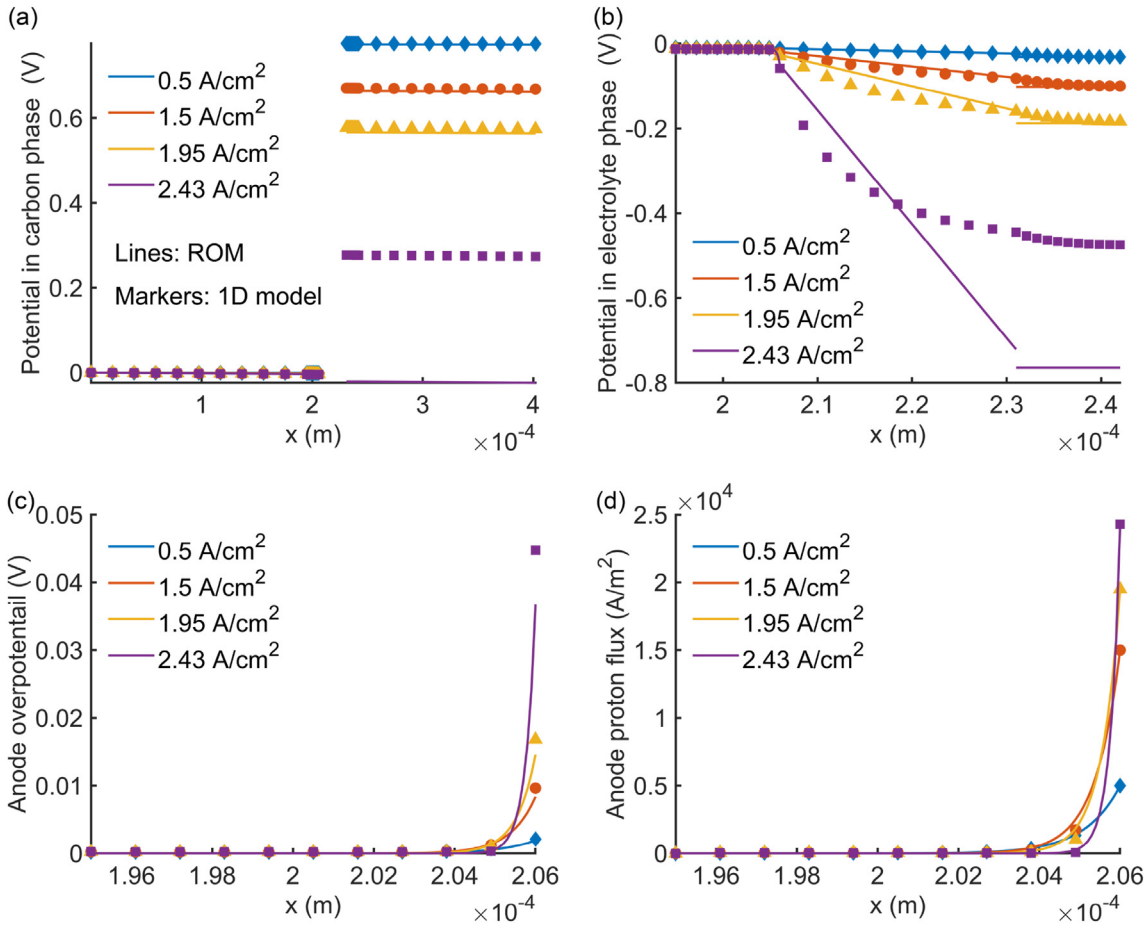

Fig. 4 – Predicted potential distribution and proton flux under the base condition: (a) potential in carbon phase; (b) potential in electrolyte phase; (c) proton flux in anode ionomer; (d) anode overpotential of the hydrogen oxidation reaction.

Another possible factor influencing the limiting current is the air/fuel starvation, and the molar fractions of oxygen and hydrogen in the electrodes are shown in Fig. 6. The decreasing trend of oxygen and hydrogen are both predicted by the ROM with high accuracy and the concentration of them at the CL catalyst surface is sufficient to support a stable reversible potential and fast reaction kinetics. From Fig. 6, it can also be inferred that oxygen starvation will happen before hydrogen, and that the limiting current due to oxygen starvation can be roughly estimated as around 5 A/cm^2. However, as the effective oxygen diffusion coefficient is also influenced by the liquid water saturation, and the limiting current can also be restricted by reactant diffusion in the ionomer, this estimated limiting current can be much higher than that seen in practice. The high precision of the gas diffusion sub-model also indicates that the slight error of liquid water saturation has little impact on the simulated cell performance.

From Figs. 3–6, it can be concluded that the predicted cell performance and internal status of the ROM agree well with the 1D model under a wide range of working conditions - until approaching 95% of the limiting currents. Both the limiting current itself and the error of the limiting current are not caused by the exhaustion of oxygen or fuel but by the membrane dehydration and its resulting increased resistance, and the largest error happens at the anode/membrane interface. In addition, the temperature – ionomer hydration condition relationship also indicates that the errors of the sub-models can form a positive feedback loop, and that oversimplified sub-models without the approximation methods developed in this work can lead to large errors compared to the full 1D model.

Model-based structural design of MEA

The development of PEMFC components with superior transport and electrochemical properties is a popular field of study. However, even for commercial PEMFC components with similar material properties, their geometric properties, especially the thickness of individual layers, can affect the overall performance of the cell significantly, and a quantitative analysis is required to determine their contributions and coupling effects. Here we demonstrate the applicability and extensibility of our model by using the model for structural design of the MEA. Oxygen transport in the CL ionomer is one of the main sources of O_2 transport resistance and can be especially important for ultra-thin CLs [20]. Thus in this section, our model is extended to incorporate the agglomerate sub-model for cathode CL detailed elsewhere [11,23] to account for this mechanism. The details of the CL sub-model and the model parameters are summarized in Table 7

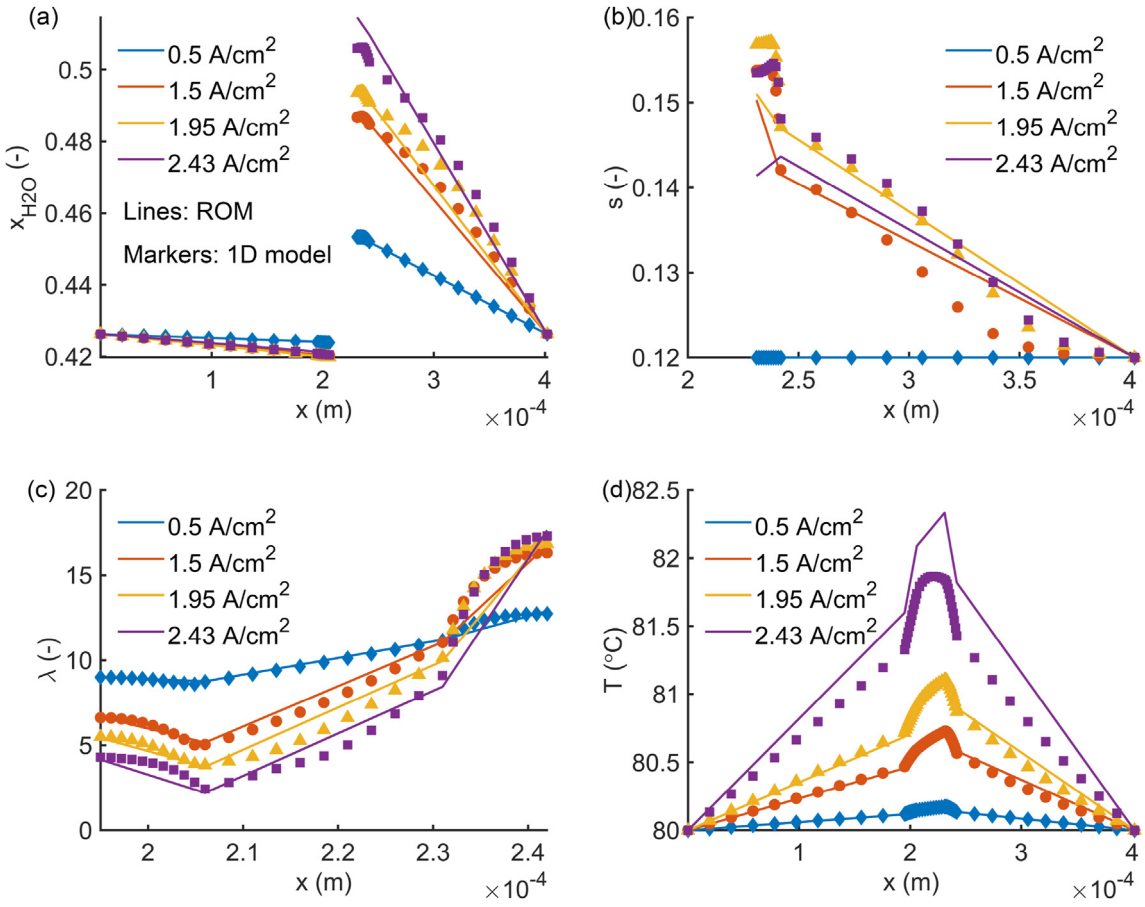

Fig. 5 – Predicted water transport status and internal temperature profile under the base condition: (a) molar fraction of water vapor; (b) liquid water saturation in cathode CL and GDL; (c) ionomer water content; (d) temperature distribution.

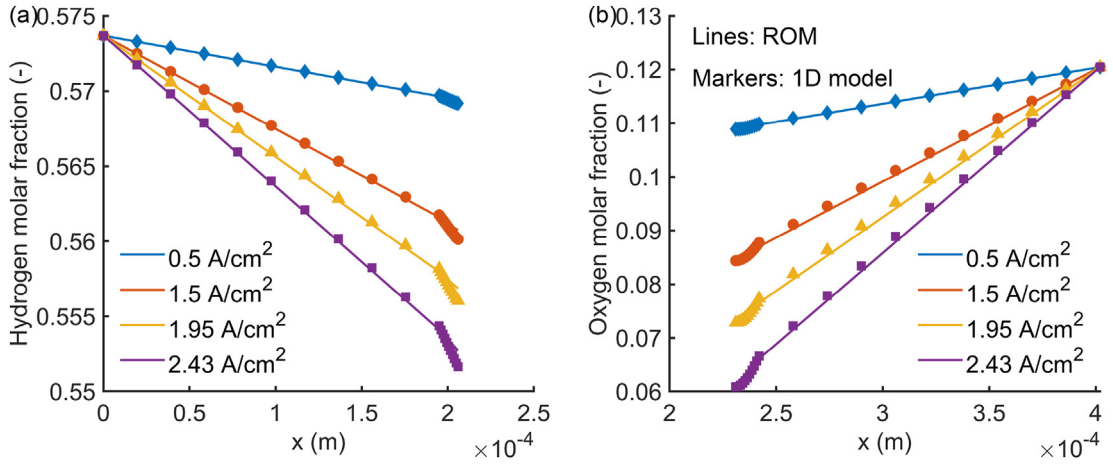

Fig. 6 – Molar fraction of oxygen and fuel: (a) hydrogen molar fraction in anode electrode; (b) oxygen molar fraction in cathode electrode.

[11,23]. As shown in Fig. 7, our model results agree well with the experimental data, with the performance loss due to increased mass transport resistance of thinner CL successfully captured.

Then, a detailed analysis of the thickness of PEMFC layers is presented with the modified model. The model parameters of the thick CL case are considered as the 'base case' and the investigated ranges of them can be found in Table 8.

First, the overall cell performance under 50% and 200% thickness of individual layers is investigated and the results can be found in Fig. 8. It can be observed that among all three types of layers, the thickness of the membrane has the largest

Table 7 – Equations of the agglomerate sub-model [11,23] and the model parameters.

Equations of the agglomerate sub-model	
Thiele modulus	$\beta = \frac{d_{agg}}{6}\sqrt{\frac{q_C}{D^{eff}_{O_2,agg}}}$
Agglomerate effective factor	$Er = \frac{1}{\beta}\left(\frac{1}{\tanh(3\beta)} - \frac{1}{3\beta}\right)$
Cathode half cell reaction constant	$q_C = \frac{a i_{0,C}(1-\theta_{PtO})}{4F(1-\varepsilon_{p,CL})C^{ref}_{O_2}}\left[\exp\left(\frac{F}{RT}\eta\right) - \exp\left(-\frac{F}{RT}\eta\right)\right]$
Cathode catalyst layer current density	$I = 4FL_{CCL}\frac{P_{O_2}}{h_{O_2}}\left[\frac{1}{q_C Er(1-\varepsilon_{p,CL})} + \frac{(d_{agg}+2\delta_{agg})\delta_{agg}}{a_{agg}d_{agg}D_{O_2,film}}\right]^{-1}$
Platinum oxide formation	$\frac{\partial\theta_{PtO}}{\partial t} = 0.0128\ s^{-1}(1-\theta_{PtO})\exp\left(\frac{F}{2RT}\eta_{PtO} - \frac{10\ kJ/mol}{RT}\theta_{PtO}\right) - 0.0128\ s^{-1}\theta_{PtO}\exp\left(-\frac{F}{2RT}\eta_{PtO}\right)$
Overpotential of PtO formation, η_{PtO} (V)	$\eta_{PtO} = \phi_e - \phi_p - U_{0,PtO}$
Added or changed model parameters	
Cathode exchange current density, $i_{0,C}$ (A/cm^2)	$i_{0,C} = i_{0,ref}\times\exp\left[\frac{67\ kJ/mol}{R}\left(\frac{1}{T_{ref}} - \frac{1}{T}\right)\right]$
Reaction coefficient of ORR, $i_{0,ref}$ (A m^{-2})	0.0208[f]
Reference concentration, $C^{ref}_{O_2}$ (mol m^{-3})	34.06
CCL thickness, L_{CCL} (m)	11×10^{-6} (thick case) [43]3.8×10^{-6} (thin case) [43]
Oxygen diffusion coefficient in ionomer, $D_{O_2,film}$ (m^2 s^{-1})	$D_{O_2,film} = (1.9f+0.11)RT\exp\left[\frac{22\ kJ/mol}{R}\left(\frac{1}{T_{ref}} - \frac{1}{T}\right)\right]\times10^{-14}\frac{mol}{Pa\cdot m\cdot s}$ [45]
Effective oxygen diffusion coefficient in agglomerate, $D^{eff}_{O_2,agg}$ (m^2 s^{-1})	$D^{eff}_{O_2,agg} = \varepsilon^{1.5}_{I,agg}D_{O_2,film}$
Agglomerate surface area, a_{agg} (m^2 m^{-3})	3.6×10^{6}[f]
Ionomer film thickness, δ_{agg} (m)	7×10^{-9}[f]
Agglomerate size, d_{agg} (m)	208×10^{-9}[f]
Ionomer fraction in agglomerate, $\varepsilon_{I,agg}$ (–)	$\varepsilon_{I,agg} = \frac{\varepsilon_{I,CL} - a_{agg}\delta_{agg}}{1-\varepsilon_{p,CL}}$
Henry's constant for oxygen, h_{O_2} (Pa m^3 mol^{-1})	$h_{O_2} = 1.33\times\exp\left(-\frac{666K}{T}\right)\times10^5\frac{Pa\cdot m^3}{mol}$ [23]
Equilibrium potential of PtO formation $U_{0,PtO}$ (V)	0.81 [11]
Proton conductivity of ionomer, σ_P (S/m)	
$\sigma_P = (0.5139\lambda - 0.326)\exp\left[1268\left(\frac{1}{303.15} - \frac{1\ K}{T}\right)\right]\times1\frac{S}{m}$ [39]	

[f] Fitted.

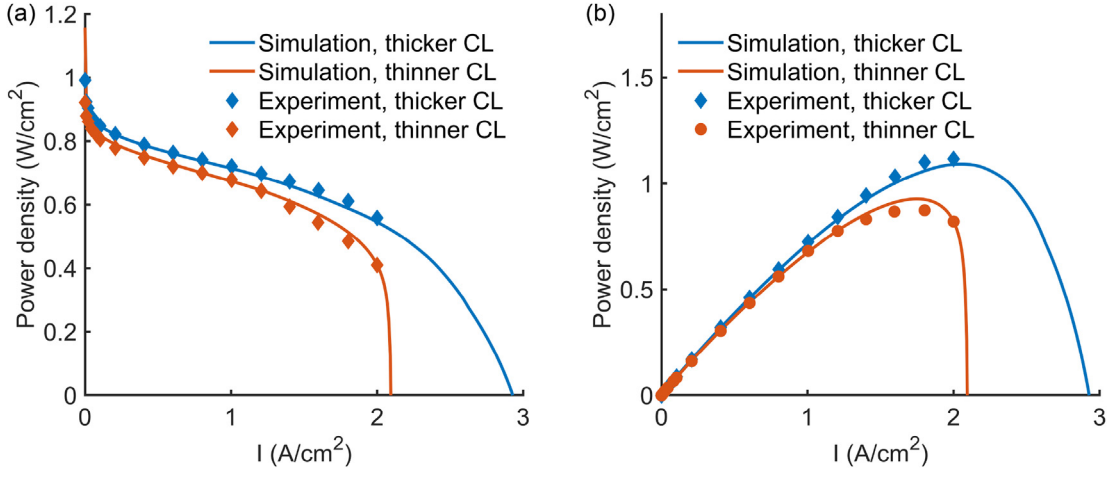

Fig. 7 – Comparison of simulation and experimental results of different CL thickness from Ref. [43]: (a) polarization curves; (b) power density curves.

Table 8 – Investigated design parameters and their ranges.

Parameter	Base case		Range
	Anode	Cathode	
GDL thickness (μm)	195	160	20%–200%
CL thickness (μm)	11	11	20%–200%
Membrane thickness (μm)	25		20%–200%

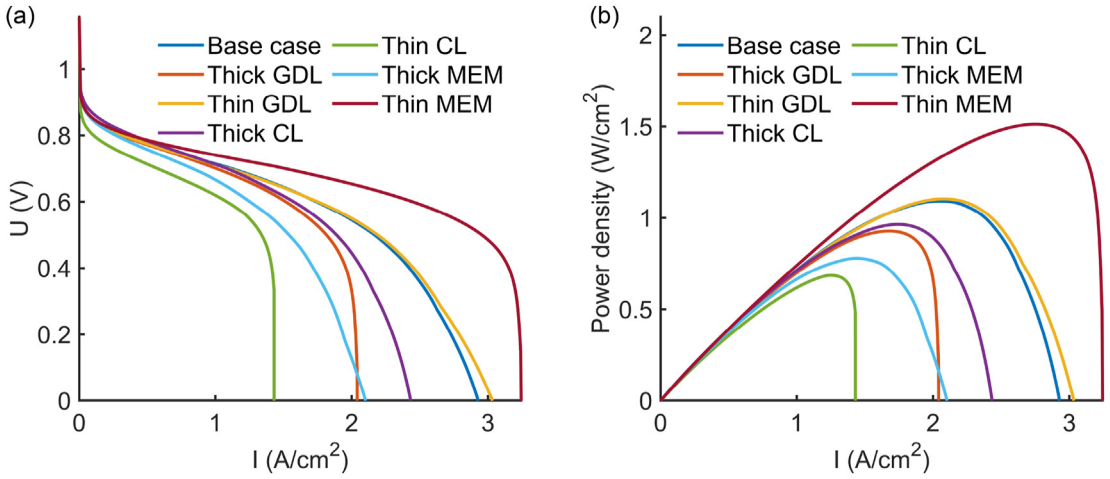

Fig. 8 – Cell performance under the base case, 20% thickness of individual layers and 200% thickness of individual layers: (a) polarization curves; (b) power density curves.

impact. Both thinner GDLs and a thinner electrolyte membrane provide better cell performance, but the effect of thin GDLs is limited as water management becomes the dominant factor instead of the transport of oxygen. On the other hand, both thinner and thicker CLs influence the cell performance negatively. Thinner CLs have lower electrochemical surface area and worse local oxygen transport, leading to the lowest cell performance. Although thicker CLs increase the electrochemical surface area (ECSA) and can slightly improve the ORR reaction kinetics at lower current density, they lead to water management problems and higher Ohmic resistance. It should also be noted that while the cell showed the best performance with an ultra-thin membrane thickness, thinner membranes have worse mechanical strength [46] and can result in significantly increased gas crossover rate in practice [46,47], which is not considered in this model. Any crossover of hydrogen reduces the open circuit voltage of the cell [12] and the crossover of nitrogen can dilute the anode stream [47]. In addition to reducing cell performance, oxygen diffusing through the membrane can further increase the production of hydrogen peroxide [12], which is detrimental to both the membrane and GDL [12,48], thus thinner membrane can also lead to durability problems, leading to a minimum electrolyte thickness in practice.

Fig. 9 presents six performance indexes across the range of layer thicknesses, including voltages at two different current densities, limiting current, peak power density and volumetric power density, and power density at 0.75 V. Compared to the GDL and electrolyte membrane, the thickness of CL has the largest influence on the voltage at low current density, which can be improved considerably with a thicker catalyst layer. On the other hand, the influence of the membrane thickness also becomes significant at a moderate current density of 1.2 A/cm^2, which is shown in Fig. 9(b). Thicker CLs can slightly improve the voltage at 1.2 A/cm^2 before reaching around 120% of its initial thickness, but the worse water management of thicker CLs counters the effect of increased ECSA. For the limiting current, the thickness of all three layers becomes influential. The CL thickness is still the most important factor for thinner layers, while the effect of GDL and membrane thickness are greater for thicker cases. As shown in Fig. 9(d), the peak power of the cell follows nearly the same trend as the limiting current density, except for the thinner membrane, as the limiting current of the thinner membrane case is limited by the oxygen transport resistance. While thicker GDLs hinder oxygen transport, they can lock more water inside the cathode CLs which leads to a better hydrated membrane. This coupled effect causes the peak power density to be optimized at around 70% of the initial GDL thickness. Fig. 9(e) shows the peak volumetric power density, which is calculated with an assumed bipolar plate thickness of 2 mm. The influence of membrane and CL thickness on it is almost the same as Fig. 9(d), as their thicknesses are negligible compared to the plates. The GDL, however, is the thickest part of the MEA, thus thinner GDLs lead to higher volumetric density even if it reduces the maximum power output per MEA surface area. As the fuel cell operates at a higher efficiency under higher voltage output, the power at high voltage can also be considered as an important performance index, and the power density at 0.75 V is shown in Fig. 9(f). Similar to the impact on voltage at 1.2 A/cm^2, both thin and thick GDLs have negative effects. The power density at high voltage is significantly

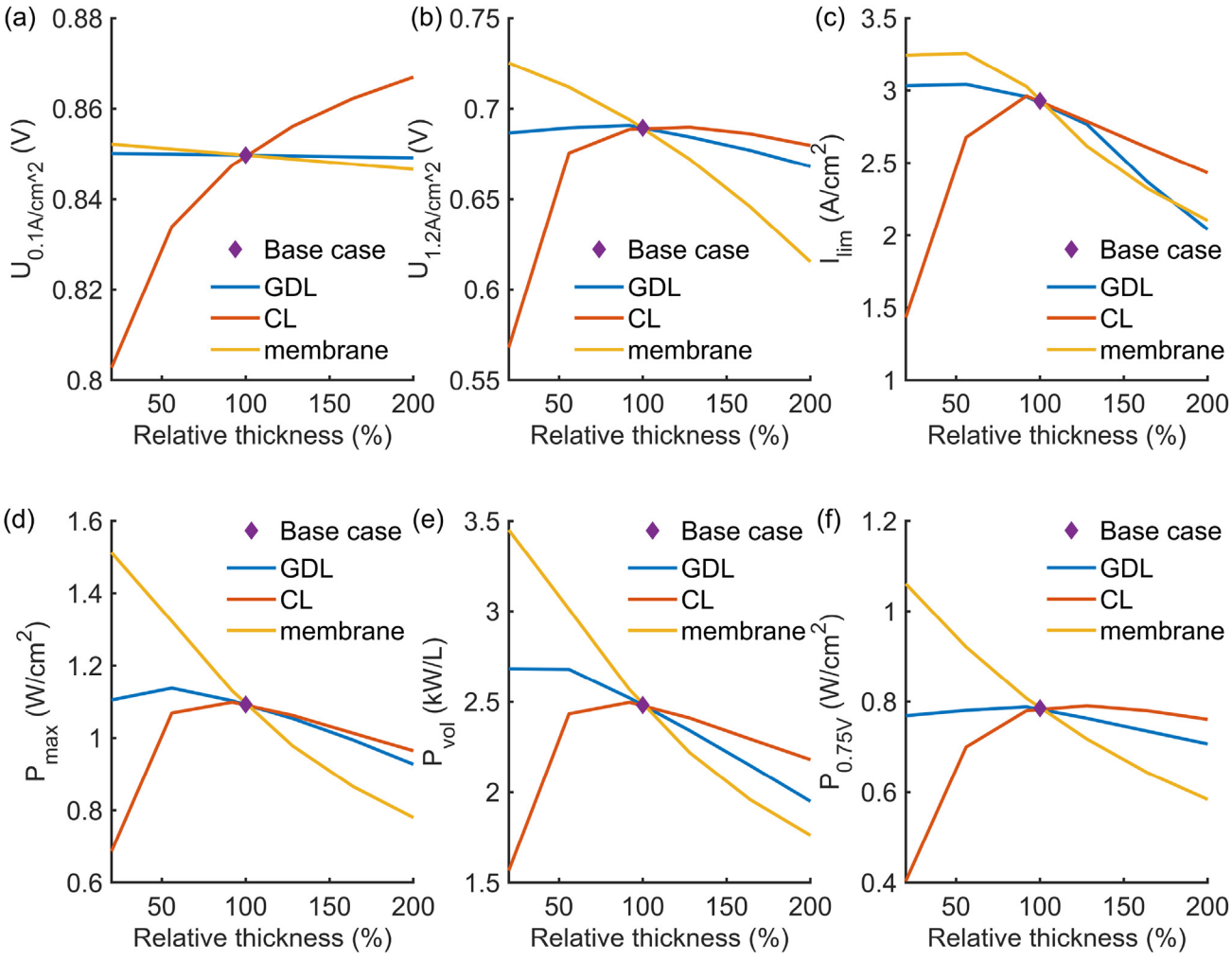

Fig. 9 – Cell performance under different layer thicknesses: (a) voltage at 0.1 A/cm^2; (b) voltage at 1.5 A/cm^2; (c) limiting current; (d) maximum power density; (e) maximum volumetric power density; (f) power density at 0.75 A/cm^2.

lower for thinner CLs due to the reduced Pt content and increased local O_2 transport flux, but increasing CL thickness to more than 120% of its initial value cannot further increase cell performance.

The changes of internal state induced by the layer thicknesses are also analyzed. Fig. 10 shows the internal statuses under limiting current (at 0 V). Fig. 10(a) shows the minimum membrane hydration status. The minimum ionomer water content at limiting current is increased for thinner CLs/membrane and thicker GDLs, as the oxygen transport limitation becomes the dominant factor of limiting current under these cases. Since the membrane conductivity follows a linear relationship with its hydration status, the trend shown in Fig. 10(b) is opposite to Fig. 10(a). From Fig. 10(c), it can be observed that both thicker CLs and membranes can reduce the liquid water inside the cell due to a lowered limiting current, but thicker GDLs can significantly increase the liquid water locked in the cell. It should also be noted that as the gas in the cathode CLs can become less saturated at limiting current due to elevated temperature gradient, the liquid water saturation shown in Fig. 10(c) does not always represent its maximum value. Fig. 10(d) shows the highest temperature rise. Although thicker layers can result in a higher heat transfer resistance, thicker membranes and CLs reduce the limiting current significantly and cause a reduced temperature gradient. However, since the GDLs has a smaller influence on the limiting current, thicker GDLs can still lead to a higher temperature difference inside the cell. Due to the same effect, thicker CLs and membrane can increase the minimum hydrogen and oxygen concentration in the catalyst layer at limiting current, as shown in Fig. 10(e) and (f), respectively. Fig. 9(g) and (h) show the highest anode and cathode overpotential, respectively. It can be found that at limiting current, the highest anode overpotential is around 7% of the cathode overpotential under the base case. Due to the lowered limiting current of thicker CLs and membranes, the overpotentials of electrochemical reactions are also reduced under these two cases. Since the HOR has a relatively large reaction coefficient and the hydrogen concentration is higher than oxygen, the peak anode overpotential is mostly dependent on the ionomer proton conductivity instead of the H_2 concentration, therefore the increased H_2 concentration due to thinner GDLs has little influence on the anode overpotential. On the other hand, the ORR has sluggish reaction kinetics and the cathode overpotential is governed by the O_2 concentration. Thicker GDLs and thinner CLs increases oxygen transport resistance thus

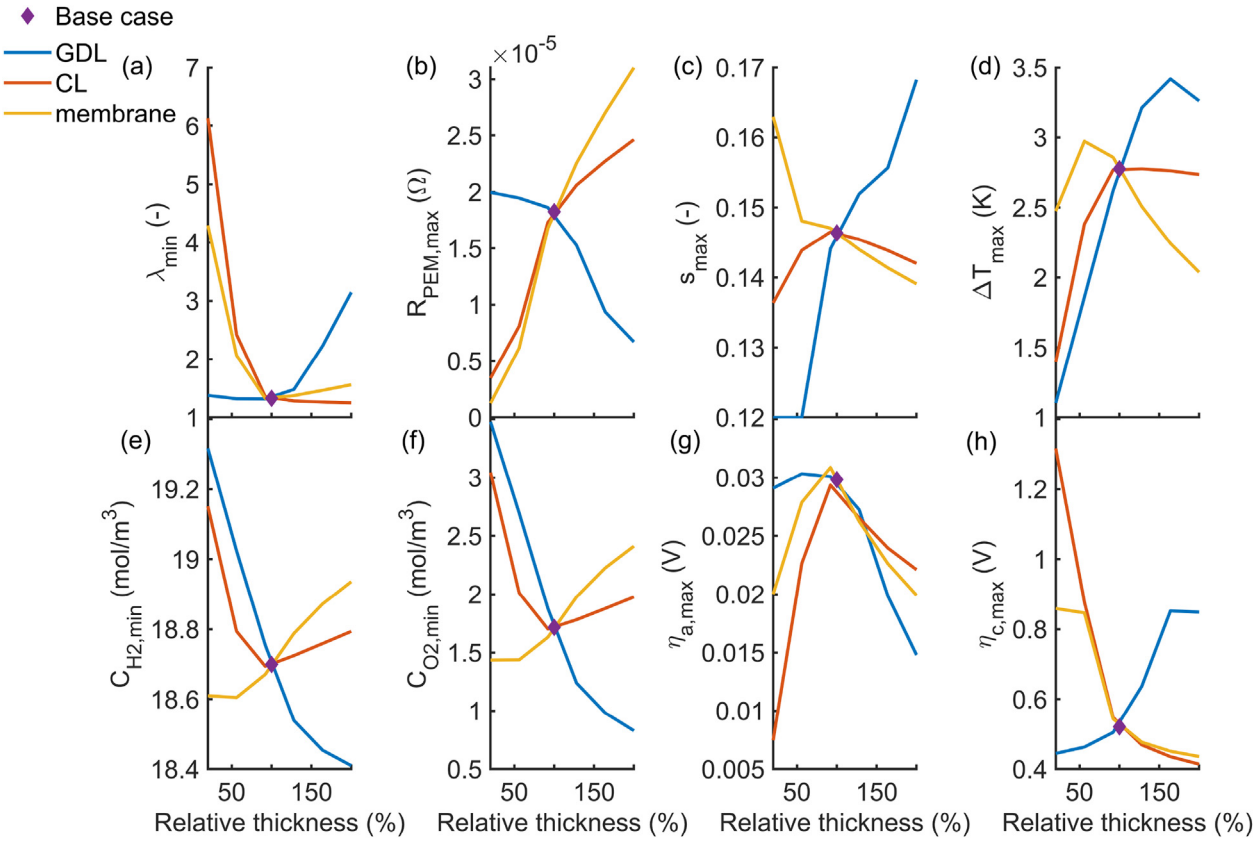

Fig. 10 – Internal cell states at the limiting current density: (a) minimum membrane water content; (b) maximum membrane resistance; (c) maximum liquid water saturation; (d) largest temperature rise; (e) lowest hydrogen concentration; (f) lowest oxygen concentration; (g) peak anode overpotential; (h) peak cathode overpotential.

can lead to significantly larger cathode overpotential, while the increased overpotential for thinner membrane is due to the larger current density. By comparing Fig. 10(b) and (h), it can be clearly observed that the dominant factor of limiting current transitions from membrane dehydration to oxygen transport limitation for thick GDLs, thin membranes, and thin CLs.

From Figs. 7–10, it can be concluded that both oxygen transport and membrane humidification can have a large impact on cell performance, but that the dominant factor can be different for different component thicknesses. In addition, although there is already a trend towards thinner MEA layers, the above discussions show that reducing the layer thicknesses may not always improve cell performance, and that

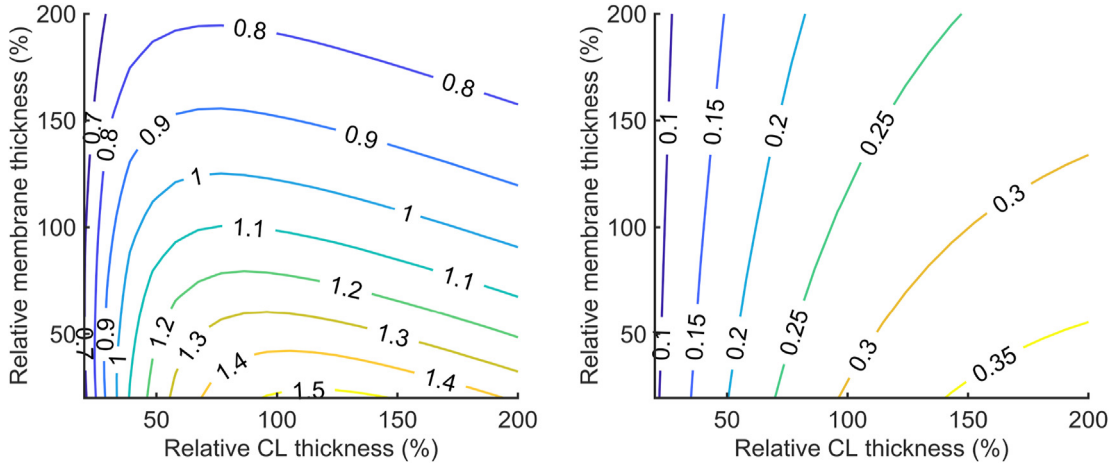

Fig. 11 – Contour map of power density (in W/cm^2) under different CL and membrane thicknesses: (a) maximum power density; (b) power density at 0.8 V.

the cell configuration can be optimized for a given performance target. Considering both power capability and cell efficiency, here we target two performance indexes, namely the maximum power density and power density at 0.8 V, and contour maps of them are shown in Fig. 11(a) and Fig. 11(b) respectively. Both the maximum power density and power density at 0.8 V increase with a thinner membrane, but the highest maximum power density happens at around 120% of initial CL thickness, while the power density can be improved with thicker CLs. With Fig. 11, the thicknesses of CLs and membrane can be optimized for given performance indexes. For instance, if a maximum power density of 1.4 W/cm^2 and a power density of 0.3 W/cm^2 are required, the CL thickness should be within the range of 95%–190% of its initial thickness, and the membrane needs to be thinner than 40% of its thickness under the base case.

Conclusions

In this paper, a ROM which can achieve similar accuracy as the 1D model with significantly lower computational cost is presented. An order reduction method is developed to reduce the 1D descriptions of conservation equations to six computing nodes located at the boundaries of the cell components. Then, the lumped transport properties between the nodes are computed with a discretized approximation method. Due to the different reaction kinetics of HOR and ORR, two sub-models, namely a simplified 1D anode electrochemical model and a lumped cathode model, are used to describe the CL electrochemistry. To avoid large errors induced by water transport, an analytical approximation method is also established to capture the water content distribution in the membrane.

The accuracy of the developed model is then validated against the original 1D model and experimental data in the literature. Comparing to the experimental result of Ref. [43] under baseline conditions, both the ROM and 1D model predict the polarization curve of the cell with high precision. The simulation results of the ROM are also compared with the 1D model under wide ranges of operating conditions. The comparison shows that the accuracy of the ROM is very close to the 1D model, and that the computing time of the developed model is around two magnitudes lower than the original 1D approach. The error of the ROM is kept under 4% for most of working conditions, but the error tends to increase when the cell is less humidified. The analysis of internal status also shows that the ROM can provide similar information of the scalars at the computing nodes. It is also revealed that the slight discrepancy between the ROM and the original 1D model at limiting current is due to the small error of membrane dehydration and the nonlinear relationship between membrane hydration status and proton conductivity.

To further demonstrate the applicability and extensibility of the model approach, the base-case model is extended to incorporate the cathode CL agglomerate sub-model and used for a parametric study to investigate the influence of cell component thickness on the cell performance. The model shows good agreement with the experimental data for different CL thicknesses. The results of the parametric study show that the thickness of the CL dominates the voltage drop at low current density and that the influence of membrane and GDL thickness also becomes considerable with increasing load. The analysis of internal status of the cell shows that the dominant factor of cell performance changes from membrane dehydration to oxygen transport for thicker GDLs and thinner membrane/CLs. The contour maps of power density under different CL and membrane thicknesses show that to optimize the maximum power density and the cell performance at higher efficiency, the thickness of membrane needs to be reduced by 60% while the CL thickness needs to be restricted to 95%–190% of its initial value.

Declaration of competing interest

The authors declare that they have no known competing financial interests or personal relationships that could have appeared to influence the work reported in this paper.

Acknowledgements

This research did not receive any specific grant from funding agencies in the public, commercial, or not-for-profit sectors.

REFERENCES

[1] Wang Y, Ruiz Diaz DF, Chen KS, Wang Z, Adroher XC. Materials, technological status, and fundamentals of PEM fuel cells – a review. Mater Today 2020;32:178–203.
[2] Pan M, Pan C, Li C, Zhao J. A review of membranes in proton exchange membrane fuel cells: transport phenomena, performance and durability. Renew Sustain Energy Rev 2021;141:110771.
[3] Zhang D, Bertei A, Tariq F, Brandon N, Cai Q. Progress in 3D electrode microstructure modelling for fuel cells and batteries: transport and electrochemical performance. Progress in Energy 2019;1:012003.
[4] Ira Y, Bakhshan Y, Khorshidimalahmadi J. Effect of wettability heterogeneity and compression on liquid water transport in gas diffusion layer coated with microporous layer of PEMFC. Int J Hydrogen Energy 2021;46:17397–413.
[5] Sui P-C, Zhu X, Djilali N. Modeling of PEM fuel cell catalyst layers: status and outlook. Electrochemical Energy Reviews 2019;2:428–66.
[6] Weber AZ, Borup RL, Darling RM, Das PK, Dursch TJ, Gu W, et al. A Critical review of modeling transport phenomena in polymer-electrolyte fuel cells. J Electrochem Soc 2014;161:F1254–99.
[7] Vetter R, Schumacher JO. Free open reference implementation of a two-phase PEM fuel cell model. Comput Phys Commun 2019;234:223–34.
[8] Nanadegani FS, Lay EN, Iranzo A, Salva JA, Sunden B. On neural network modeling to maximize the power output of PEMFCs. Electrochim Acta 2020;348:136345.
[9] Ma R, Yang T, Breaz E, Li Z, Briois P, Gao F. Data-driven proton exchange membrane fuel cell degradation predication through deep learning method. Appl Energy 2018;231:102–15.
[10] Das PK, Li X, Liu Z-S. Analytical approach to polymer electrolyte membrane fuel cell performance and optimization. J Electroanal Chem 2007;604:72–90.

[11] Futter GA, Gazdzicki P, Friedrich KA, Latz A, Jahnke T. Physical modeling of polymer-electrolyte membrane fuel cells: understanding water management and impedance spectra. J Power Sources 2018;391:148–61.
[12] Futter GA, Latz A, Jahnke T. Physical modeling of chemical membrane degradation in polymer electrolyte membrane fuel cells: influence of pressure, relative humidity and cell voltage. J Power Sources 2019;410-411:78–90.
[13] Xing L, Cai Q, Xu C, Liu C, Scott K, Yan Y. Numerical study of the effect of relative humidity and stoichiometric flow ratio on PEM (proton exchange membrane) fuel cell performance with various channel lengths: an anode partial flooding modelling. Energy 2016;106:631–45.
[14] Ye Q, Nguyen TV. Three-dimensional simulation of liquid water distribution in a PEMFC with experimentally measured capillary Functions. J Electrochem Soc 2007;154:B1242.
[15] Zhang G, Fan L, Sun J, Jiao K. A 3D model of PEMFC considering detailed multiphase flow and anisotropic transport properties. Int J Heat Mass Tran 2017;115:714–24.
[16] Vetter R, Schumacher JO. Experimental parameter uncertainty in proton exchange membrane fuel cell modeling. Part I: Scatter in material parameterization. J Power Sources 2019;438:227018.
[17] Vetter R, Schumacher JO. Experimental parameter uncertainty in proton exchange membrane fuel cell modeling. Part II: Sensitivity analysis and importance ranking. J Power Sources 2019;439:126529.
[18] Liu J, García-Salaberri PA, Zenyuk IV. The impact of reaction on the effective properties of Multiscale Catalytic porous Media: a case of polymer electrolyte fuel cells. Transport Porous Media 2019;128:363–84.
[19] Liu J, García-Salaberri PA, Zenyuk IV. Bridging scales to model reactive diffusive transport in porous Media. J Electrochem Soc 2020;167.
[20] Sánchez-Ramos A, Gostick JT, García-Salaberri PA. Modeling the effect of low Pt loading cathode catalyst layer in polymer electrolyte fuel cells: Part I. Model formulation and validation. J Electrochem Soc 2021:168.
[21] Sánchez-Ramos A, Gostick J, García-Salaberri P. Modeling the effect of low Pt loading cathode catalyst layer in polymer electrolyte fuel cells. Part II: parametric analysis. J Electrochem Soc 2022;169:074503.
[22] Salari S, Stumper J, Bahrami M. Direct measurement and modeling relative gas diffusivity of PEMFC catalyst layers: the effect of ionomer to carbon ratio, operating temperature, porosity, and pore size distribution. Int J Hydrogen Energy 2018;43:16704–18.
[23] Moein-Jahromi M, Kermani MJ. Performance prediction of PEM fuel cell cathode catalyst layer using agglomerate model. Int J Hydrogen Energy 2012;37:17954–66.
[24] Xing L, Mamlouk M, Kumar R, Scott K. Numerical investigation of the optimal Nafion® ionomer content in cathode catalyst layer: an agglomerate two-phase flow modelling. Int J Hydrogen Energy 2014;39:9087–104.
[25] Ju H, Meng H, Wang C-Y. A single-phase, non-isothermal model for PEM fuel cells. Int J Heat Mass Tran 2005;48:1303–15.
[26] Gößling S, Nickig N, Bahr M. 2-D + 1-D PEM fuel cell model for fuel cell system simulations. Int J Hydrogen Energy 2021;46:34874–82.
[27] Wang M, Ding Y, Hu J, Xu L, Yang X. Numerical simulation of water and heat transport in the cathode channel of a PEM fuel cell. Int J Hydrogen Energy 2022;47:11007–27.
[28] Yong Z, Shirong H, Xiaohui J, Yuntao Y, Mu X, Xi Y. Performance study on a large-scale proton exchange membrane fuel cell with cooling. Int J Hydrogen Energy 2022;47:10381–94.
[29] Ashrafi H, Pourmahmoud N, Mirzaee I, Ahmadi N. Performance improvement of proton-exchange membrane fuel cells through different gas injection channel geometries. Int J Energy Res 2022;46:8781–92.
[30] Jabbary A, Rostami Arnesa S, Samanipour H, Ahmadi N. Numerical investigation of 3D rhombus designed PEMFC on the cell performance. Int J Green Energy 2021;18:425–42.
[31] Tan Q, Lei H, Liu Z. Numerical simulation analysis of the performance on the PEMFC with a new flow field designed based on constructal-theory. Int J Hydrogen Energy 2022;47:11975–90.
[32] Zheng L, Hou Y, Zhang T, Pan X. Performance prediction of fuel cells using long short-term memory recurrent neural network. Int J Energy Res 2021;45:9141–61.
[33] Wang B, Zhang G, Wang H, Xuan J, Jiao K. Multi-physics-resolved digital twin of proton exchange membrane fuel cells with a data-driven surrogate model. Energy and AI 2020;1:100004.
[34] Wang F-K, Cheng X-B, Hsiao K-C. Stacked long short-term memory model for proton exchange membrane fuel cell systems degradation. J Power Sources 2020;448:227591.
[35] Bressel M, Hilairet M, Hissel D, Ould Bouamama B. Model-based aging tolerant control with power loss prediction of Proton Exchange Membrane Fuel Cell. Int J Hydrogen Energy 2020;45:11242–54.
[36] Bressel M, Hilairet M, Hissel D, Ould Bouamama B. Extended Kalman Filter for prognostic of proton exchange membrane fuel cell. Appl Energy 2016;164:220–7.
[37] Ferreira RB, Falcão DS, Oliveira VB, Pinto AMFR. 1D + 3D two-phase flow numerical model of a proton exchange membrane fuel cell. Appl Energy 2017;203:474–95.
[38] Xie B, Zhang G, Jiang Y, Wang R, Sheng X, Xi F, et al. "3D+1D" modeling approach toward large-scale PEM fuel cell simulation and partitioned optimization study on flow field. eTransportation 2020;6:100090.
[39] Jiang Y, Yang Z, Jiao K, Du Q. Sensitivity analysis of uncertain parameters based on an improved proton exchange membrane fuel cell analytical model. Energy Convers Manag 2018;164:639–54.
[40] Rahman MA, Mojica F, Sarker M, Chuang P-YA. Development of 1-D multiphysics PEMFC model with dry limiting current experimental validation. Electrochim Acta 2019;320:134601.
[41] Thompson EL, Jorne J, Gu W, Gasteiger HA. PEM fuel cell operation at −20°C. II. Ice formation Dynamics, current distribution, and voltage Losses within electrodes. J Electrochem Soc 2008;155:B887.
[42] Neyerlin KC, Gu W, Jorne J, Clark A, Gasteiger HA. Cathode catalyst Utilization for the ORR in a PEMFC. J Electrochem Soc 2007;154:B279.
[43] Ono Y, Mashio T, Takaichi S, Ohma A, Kanesaka H, Shinohara K. The analysis of performance loss with low Platinum loaded cathode catalyst layers. ECS Trans 2010;28:69–78.
[44] Sadeghifar H, Djilali N, Bahrami M. Effect of Polytetrafluoroethylene (PTFE) and micro porous layer (MPL) on thermal conductivity of fuel cell gas diffusion layers: modeling and experiments. J Power Sources 2014;248:632–41.
[45] Weber AZ, Newman J. Transport in polymer-electrolyte membranes. J Electrochem Soc 2004:151.
[46] Ehlinger VM, Kusoglu A, Weber AZ. Modeling coupled durability and performance in polymer-electrolyte fuel cells: membrane effects. J Electrochem Soc 2019;166:F3255–67.
[47] Kienitz B. Optimizing polymer electrolyte membrane thickness to maximize fuel cell vehicle range. Int J Hydrogen Energy 2021;46:11176–82.
[48] Liu H, George MG, Messerschmidt M, Zeis R, Kramer D, Scholta J, et al. Accelerated degradation of polymer electrolyte membrane fuel cell gas diffusion layers. J Electrochem Soc 2017;164:F695–703.